Experimental Demonstration of Scanned Spin-Precession Microscopy

V. P. Bhallamudi,[1,*] C. S. Wolfe,[1] V. P. Amin,[2] D. E. Labanowski,[1] A. J. Berger,[1] D. Stroud,[1] J. Sinova,[2] and P. C. Hammel[1]

[1]*Department of Physics, The Ohio State University, Columbus, Ohio 43210, USA*
[2]*Department of Physics and Astronomy, Texas A&M University, College Station, Texas 77843, USA*
(Received 23 May 2013; published 10 September 2013)

We present a new tool for imaging spin properties. We show that a spatially averaged spin signal, measured as a function of a scanned magnetic probe's position, contains information about the local spin properties. In this first demonstration we map the injected spin density in GaAs by measuring spin photoluminescence with a resolution of 1.2 μm. The ultimate limit of the technique is set by the gradient of the probe's field, allowing for a resolution beyond the optical diffraction limit. Such probes can also be integrated with other detection methods. This generality allows the technique to be extended to buried interfaces and optically inactive materials.

Interest in spin physics and spintronic device development [1–3] has driven an explosion in device geometries and material choices. However, the principal spin microscopy tools for spintronic materials are primarily based on optical detection [4,5], and are thereby limited to certain materials. Scientists studying spin phenomena will need a multitude of characterization tools to address sensitive spin detection in new materials and device structures [6–10]. Magnetic resonance force microscopy [11,12], for example, offers sensitive detection of spin moments that are localized or nearly so, and requires a high vacuum, cryogenic environment. Magnetometry based on nitrogen-vacancy centers in diamond [13–15] is a powerful approach if one can bring the spin system into intimate contact with a nitrogen-vacancy-containing diamond surface or a scanned diamond microstructure, allowing for measurements of the fields generated by the spin system. Spin-polarized scanning tunneling microscopy [16] perhaps provides the best spatial resolution among spin detection techniques, but typically requires ultrahigh vacuum conditions and is limited to studying surfaces.

Here we demonstrate a new type of imaging technique, which we call scanned spin-precession microscopy, that is complementary to these other techniques. It offers the advantage of using the preferred detection method for the spins in their intended environment. This can enable the study of devices with buried interfaces and materials that are not optically active. Our approach can enhance the imaging capabilities of the few well-established spin detection techniques, such as Kerr or Faraday microscopy, or provide one where none exists, e.g., in the case of electrical detection.

We combine standard spin detection techniques with the idea of encoding spatial information using magnetic field gradients provided by a micromagnetic probe (henceforth called the probe), akin to magnetic resonance imaging (MRI). By understanding the effects of this gradient on the spins, we are able to decode the spin information using standard deconvolution techniques.

We utilize spin precession in a magnetic field, a hallmark characteristic of a magnetic moment, such as used in Hanle effect measurements [17]. The encoding is achieved by selectively precessing spins in a localized region underneath the probe via its inhomogeneous magnetic field. This effect is illustrated in the simulations shown in Fig. 1. Such a local perturbation with a scanned probe has been shown to be very valuable for scanned gate imaging [18,19].

For our proof-of-principle demonstration, we map the injected spin density in GaAs using spin photoluminescence (spin PL) as the detection method. We achieve a resolution of 1.2 μm, which follows from the magnetic field gradient (similar to MRI) and not from any length scale set by our optics.

Figure 2(a) shows a schematic of our experiment. We generate polarized spins, oriented along $\hat{\mathbf{z}}$, in a 1 μm thick n-GaAs membrane via the standard optical pumping method [17]. We image the resultant steady-state spin density, $\boldsymbol{\rho} = \rho(\mathbf{r}_s)\hat{\mathbf{z}}$, where $\mathbf{r}_s = (x_s, y_s, 0)$ is the position within the sample, which we treat as two dimensional. The spin density in the presence of the probe, denoted by $\mathbf{S}(\mathbf{r}_s, \mathbf{r}_p)$, will be different from $\boldsymbol{\rho}$ due to precession in the magnetic field of the probe, $\mathbf{B}_p(\mathbf{r}_p) = B_{px}\hat{\mathbf{x}} + B_{py}\hat{\mathbf{y}} + B_{pz}\hat{\mathbf{z}}$, where $\mathbf{r}_p = (x_p, y_p, z_p)$ is the position of the probe. It should be noted that in our experiment the optical pump that injects the spins is being scanned physically, while the probe is fixed. However, for our uniform sample, this is equivalent to scanning the probe relative to a fixed pump, and henceforth we will regard this to be the case. A spatially uniform transverse magnetic field $B_t\hat{\mathbf{x}}$ may also be applied to further tailor the spin precession. We repeat the imaging process with $B_t = 0.145$ T to further demonstrate the validity of this microscopy tool.

We image by measuring a spatially averaged spin-PL signal, $\Sigma(\mathbf{r}_p) \propto \int_{-\infty}^{\infty} S_z(\mathbf{r}_s, \mathbf{r}_p)d^2\mathbf{r}_s$, where S_z refers to the $\hat{\mathbf{z}}$ component of $\mathbf{S}$. More details on the measurement process are provided in the Supplemental Material [20]. Figure 2(c) shows the PL intensity for a particular
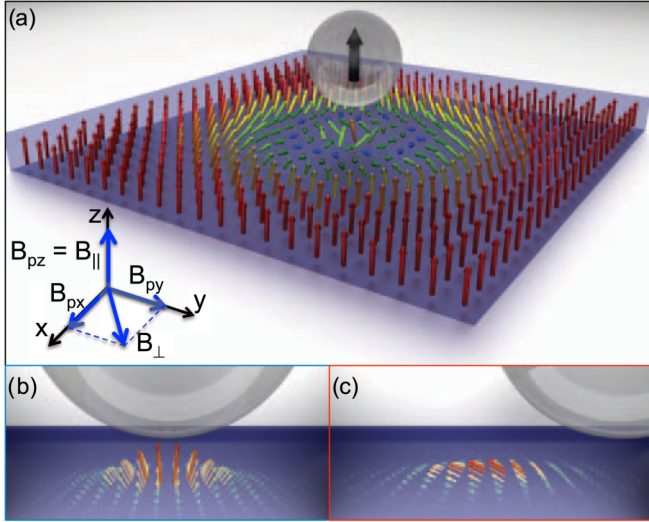
FIG. 1 (color online). The simulations shown illustrate the key physics underlying spin-precession imaging; the inhomogeneous magnetic field of a probe (sphere with black arrow, indicating the magnetization direction) generates a well-understood spatially varying dephasing of spins. Spins that are injected into a semiconducting sample reach a steady-state density resulting from a combination of the local spin properties, the injected density, and the probe's field. The arrows in all figures represent the steady-state spin density vectors **S**. The color scale represents the $\hat{z}$ component (parallel to the orientation of the injected spin) of the spins. (a) Demonstrates the case of a spatially uniform injection density and highlights the full spatial extent of the influence of the probe's field B_P. The left-hand corner shows our coordinate system (black arrows) and the various components of B_P (shorter blue arrows). Strong perpendicular fields from the probe dephase spins in an annular disk centered beneath the probe. Parallel fields immediately below the probe protect spins from dephasing. (b) and (c) show simulations identical to panel (a) except for the case of a Gaussian injection profile, corresponding to two different positions of the probe. Panels (b) and (c) correspond to the blue dot and red cross in Fig. 2(d), respectively.

$\rho = \rho_c$, measured using a spin-insensitive camera. Panels (d) and (e) show the corresponding Σ_c, for $B_t = 0$ T and 0.145 T, respectively, as a function of the probe's position.

An expression for Σ in the limit of zero diffusion (which our data show is a reasonable approximation for this experiment; more details of the derivation in the Supplemental Material [20]) is given by

$$\Sigma(\mathbf{r}_p, B_t) \propto \int_{-\infty}^{\infty}\int_{-\infty}^{\infty} S_z(\mathbf{r}_s, \mathbf{r}_p) d^2\mathbf{r}_s$$
$$\propto \int_{-\infty}^{\infty}\int_{-\infty}^{\infty} H_B(\mathbf{R}, B_t)\rho(\mathbf{r}_s) d^2\mathbf{r}_s$$
$$= H_B(\mathbf{R}, B_t) * \rho(\mathbf{r}_s), \quad (1)$$

where, $*$ represents a convolution, $\mathbf{R} = \mathbf{r}_p - \mathbf{r}_s$,

$$H_B = \frac{1}{1 + \theta_B^2(R)} \quad \text{and} \quad \theta_B^2(\mathbf{R}, B_t) = \frac{(\gamma\tau_s B_\perp(R))^2}{1 + (\gamma\tau_s B_\parallel(R))^2}.$$
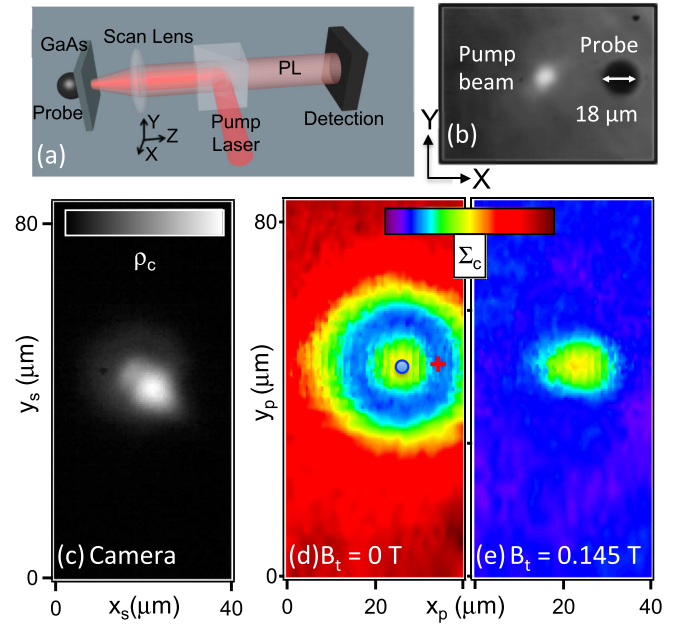

FIG. 2 (color online). (a) Schematic of the sample with pump laser and detected PL on one side, and a micromagnetic probe glued on the other side. The pump beam is scanned relative to the probe using an objective mounted on translation stages, but is equivalent to scanning the probe for our homogeneous sample. (b) Experimental optical image showing the PL spot created by the pump beam in a 1 μm thick GaAs membrane and the NdFeB probe. (c) Camera image of PL that corresponds to (and is proportional to) injection profile ρ_c. (d) The measured spin signal Σ_c (color bar) corresponding to the injection profile from panel (c), at $B_t = 0$. The location of each pixel corresponds to the relative position between the probe and the pump beam; a blue dot and red cross are included to provide two example cases. The location of the blue dot corresponds to a probe position directly above the injection beam; this configuration results in a spin density mostly pointing along the $\hat{z}$ direction [Fig. 1(b)] and gives a large signal. The red cross corresponds to a probe position 8 μm away from the center of the beam; spins precess away from the $\hat{z}$ direction due to large fields perpendicular to the injected spin direction [Fig. 1(c)] and thereby reduce the signal. (e) Σ_c for a large $B_t = 0.145$ T.

$B_\perp$ and $B_\parallel$ are, respectively, the magnitudes of the perpendicular and parallel components of the total field $\mathbf{B} = \mathbf{B}_p(\mathbf{R}) + B_t\hat{x}$ experienced by the spins. The components are defined with respect to $\hat{z}$, the orientation of injected spins. The gyromagnetic ratio denoted by γ and τ_s is the spin relaxation time. The data in Fig. 2 will be used later for obtaining H_B, which we call the precessional response function, and is the signal that would be measured for $\rho = \delta(\mathbf{r}_s)$. The expression for H_B comes from a restating of the more conventional Hanle effect, which typically only involves a spatially uniform transverse magnetic field.

As seen from the previous equations, S_z is decreased by $B_\perp$ because it causes the spins to precess away from the injected direction, resulting in a dephasing of the ensemble. On the other hand, $B_\parallel$ keeps the spins from tipping

away from the injection direction, resulting in a small θ_B and large S_z. We can view θ_B as an effective dephasing factor [21,22].

$B_\parallel$ and $B_\perp$ have distinct spatial variation in our experiments, and the consequences of their competing effects are evident in Fig. 3, where we show line scans (along $\hat{\mathbf{x}}$ and $\hat{\mathbf{y}}$) for several values of B_t. Also shown are fits obtained from Eq. (1) in which the probe is modeled as a point dipole with a moment $\mathbf{m} = m_p\hat{\mathbf{z}}$ located a height z_p above the sample (see Fig. 3 caption and the Supplemental Material [20] for more details).

The peak, marked by vertical green dashed lines at x or $y = 0$, occurs when the probe is located directly above the point of maximum injected spin density. At this point there is a maximum in $B_\parallel$ (~ 0.8 T) from the probe that preserves S_z. When the pump is far from the probe, the signal decreases with increasing B_t with a Lorentzian line shape (as expected in a Hanle measurement) whose half-width, $B_{1/2} = (\gamma\tau_s)^{-1}$, is 0.0111 T for our experiments (this is larger than expected for the doping level of our GaAs sample because the spin lifetime is limited by carrier recombination dynamics in our experiments; see Supplemental Material [20] for more information).

A second peak (blue dashed line) seen in the line scans along $\hat{\mathbf{x}}$ occurs where the $\hat{\mathbf{x}}$ component of the field from

the probe cancels B_t. As B_t is increased, this point occurs closer to the probe where its field is stronger.

The fits indicate the effectiveness of Eq. (1) in describing our data. The sensitivity of the global signal to spins at different locations relative to the probe, described by the convolution, forms the basis for imaging.

To obtain an unknown spin density ρ_u from our measured signal, the H_B needs to be determined. This can be accomplished if we first have a known ρ. We use the camera data shown in Fig. 2(a) as being proportional to ρ_c and which provides us the known ρ. Then $H_B(\mathbf{R}, B_t) = \Sigma_c(\mathbf{r}_p, B_t) \circledast \rho_c(\mathbf{r}_s)$, where we use $\circledast$ to indicate a deconvolution process. We use the Wiener algorithm [23] to implement the deconvolution. The resulting experimental H_B for both low and high B_t are shown in Figs. 4(a) and 4(b). We can also determine the H_B theoretically and these are shown in Figs. 4(c) and 4(d) for comparison; more details for obtaining them are presented in the Supplemental Material [20].

To test the fidelity of our imaging process, we now use the experimental H_B for an unknown ρ_u. We generate this ρ_u by placing a wire mesh, with wire spacing of about 0.5 mm, in front of our laser beam (see Fig. S2 in the Supplemental Material [20]). The measured Σ_u, at low and high fields, is presented in panels (a) and (c) of Fig. 5. We then extract $\rho_u(\mathbf{r}_s) = \Sigma_u(\mathbf{r}_p, B_t) \circledast H_B(\mathbf{R}, B_t)$. The extracted spin densities are shown in panels (b) and (d) of the same figure. Also shown [panel (e)], for independent verification of our imaging technique, is a camera image for the PL ($\propto \rho_u$). The line cuts present a more quantitative comparison of the extracted and measured data.

The ability to extract the spin density with both high and low B_t shows the exclusion of spurious effects, such as reflectivity changes as a function of the probe's position, in our data. Also, B_t provides a knob to optimize the H_B to suit particular imaging needs. High field imaging might provide a more intuitive H_B for the case of global
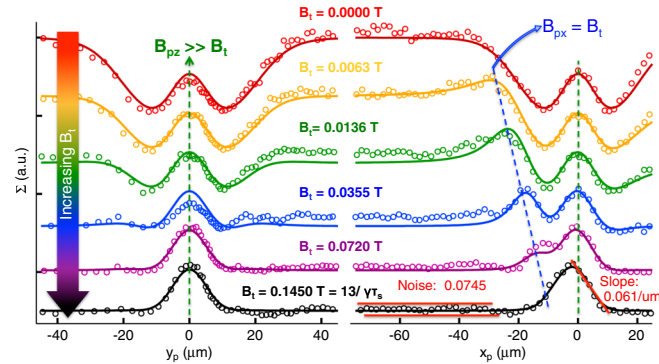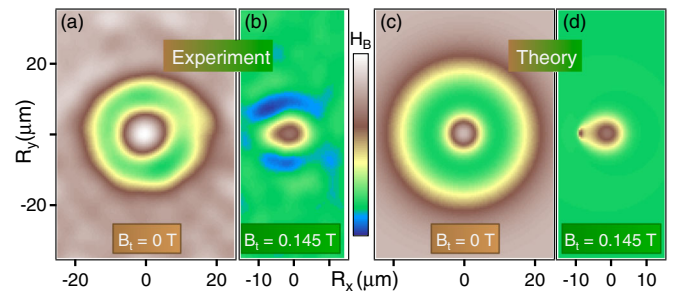

FIG. 3 (color online). Spin signal Σ_c (corresponding to ρ_c), for various B_t plotted as a function of the relative position between the pump and the probe along the $\hat{\mathbf{y}}$ (left) and the $\hat{\mathbf{x}}$ (right) directions. The data at various B_t are offset vertically for clarity. The open circles are experimental data while the solid lines represent fits obtained from Eq. (1) using $m_z = 2 \times 10^{-9}$ J/T, $z_p = 8$ μm, and $\tau_s = 2.33$ ns. The spin lifetime τ_s is obtained from Hanle measurements (see Supplemental Material [20]). The peaks marked by the green dashed lines result when the peak in ρ_c lies directly under the probe. The net parallel field directly under the probe is mostly due to B_{pz} (the $\hat{z}$ component of the probe's field) and exceeds the net transverse field (mostly given by B_t); this results in a large Σ [Eq. (1)]. The second set of peaks seen in scans along the $\hat{\mathbf{x}}$ direction (blue dashed line) occur when $B_{px} = -B_t$ (B_{px} is the $\hat{\mathbf{x}}$ component of probe's field). The resolution of our technique can be estimated by noise and slope that is seen in these line scans. For the bottom right black curve we obtain a resolution of 1.2 μm.

FIG. 4 (color online). (a) Precessional response function H_B, obtained through Wiener deconvolution of ρ_c [Fig. 2(c)] from $\Sigma_c(B_t = 0)$ [Fig. 2(d)]. (b) Experimental H_B for $B_t = 0.145$ T. (c) and (d) Theoretically derived H_B obtained from Eq. (1), using the dipole moment from the fits in Fig. 3 for $B_t = 0$ T and $B_t = 0.145$ T, respectively. The experimental H_B data have been normalized and offset to highlight the match between theory and experiment.
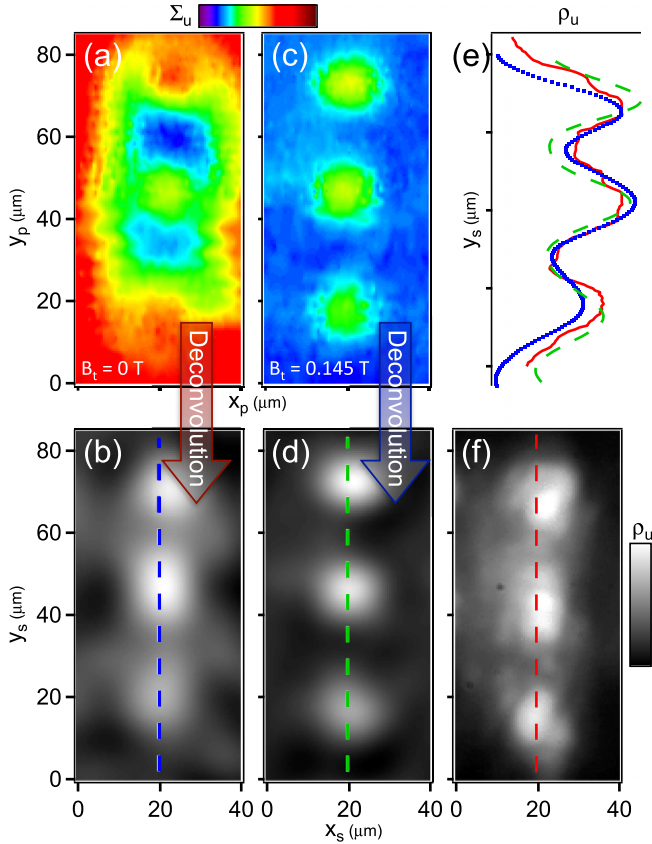
FIG. 5 (color online). Obtaining the spatial variation of an unknown spin density from the measured signal Σ: (a) Spin signal Σ_u measured for a spin density profile ρ_u (more information on how it was produced is given in the Supplemental Material [20]), with $B_t = 0$ T. (b) An image of ρ_u extracted from the Wiener deconvolution of Σ_u [panel (a)] using the experimental $H_B(B_t = 0)$ [Fig. 4(a)] as the deconvolution kernel. (c) and (d) Similarly measured Σ_u and extracted ρ_u, respectively, for $B_t = 0.145$ T. (e) Line cuts of ρ_u taken along the dashed lines in panels (b) (dotted blue) and (d) (dashed green). Also shown in solid red is a line cut from an independent camera image of ρ_u shown in panel (f).

detection. Low-field imaging may be more useful for non-local electrical devices, where a large transverse field would dephase spins before they reach the detector.

The resolution of our technique can be estimated by the ratio of noise to slope that is seen in the line scans shown in Fig. 3. We infer a spatial resolution, $\zeta \sim 1.2$ μm, in our experiment based on the sharpest change of the signal. We can also use the features seen in Fig. 5(e) to obtain an upper bound for the resolution. A Gaussian fitting of the narrowest lobe gives us $\zeta \leq 5.5$ μm. However, this is a bound that is being set by the feature size we are imaging. As in magnetic resonance imaging, the magnetic field gradient κ sets the ultimate resolution in the absence of diffusion, $\zeta = B_{1/2}/\kappa$ [21]. Gradients of up to $\sim 4 \times 10^6$ T/m have been achieved recently [11] by nanoscale fabrication of probes to submicron sizes, much smaller than ours.

These gradients are at least an order of magnitude larger than in this experiment, and should enable much finer resolution.

Resolution will be limited by diffusion, and by the unavoidable reduction of the spin signal as the region of affected spins shrinks. While diffusion can degrade the resolution, the spatial precessional response can be numerically analyzed to obtain valid and useful spatially resolved data. For large enough gradients, subdiffusion length and subdiffraction limit resolution should be achievable. Images are obtained in the presence of spin diffusion by MRI [24–26]; this should be feasible for spin precession imaging as well.

In summary, we have demonstrated a new technique for imaging spin properties using the precessional response of spins to a micromagnetic probe's field. While we have imaged variations in the spin density, the technique is more general since the response of the spins is sensitive to a variety of spin characteristics including spin lifetime [21]. Scanned spin-precession microscopy should also make it possible to image spin species with different gyromagnetic ratios, such as electrons and holes in spin devices with p-n junctions [27,28], with a resolution better than the depletion width. Work is under way to generalize the technique presented here using scannable probes mounted on cantilevers. Because of the magnetic nature of interaction between the probe and the spins, which can extend through layers of a heterostructure and a few microns deep, this tool should enable subsurface imaging. This technique should be applicable to a wide variety of materials because it relies on proven spin polarization detection techniques. With optical detection it can enhance imaging resolution, and with electrical detection it can enable imaging where none exists at present.

*bhallamudi.1@osu.edu

[1] *Special Insight Issue: Spintronics*, edited by F. Pulizzi [Nat. Mater. **11**, 367 (2012)].

[2] I. Žutić, J. Fabian, and S. Das Sarma, Rev. Mod. Phys. **76**, 323 (2004).

[3] D. D. Awschalom and M. E. Flatte, Nat. Phys. **3**, 153 (2007).

[4] J. M. Kikkawa and D. D. Awschalom, Nature (London) **397**, 139 (1999).

[5] Y. K. Kato, R. C. Myers, A. C. Gossard, and D. D. Awschalom, Science **306**, 1910 (2004).

[6] T. Sasaki, T. Oikawa, T. Suzuki, M. Shiraishi, Y. Suzuki, and K. Noguchi, Appl. Phys. Lett. **96**, 122101 (2010).

[7] W. Han, K. Pi, K. M. McCreary, Y. Li, J. I. Jared, A. G. Swartz, , and R. K. Kawakami, Phys. Rev. Lett. **105**, 167202 (2010).

[8] H. C. Koo, J. H. Kwon, J. Eom, J. Chang, S. H. Han, and M. Johnson, Science **325**, 1515 (2009).

[9] S. P. Dash, S. Sharma, R. S. Patel, M. P. de Jong, and R. Jansen, Nature (London) **462**, 491 (2009).

[10] K. Olejník, J. Wunderlich, A. C. Irvine, R. P. Campion, V. P. Amin, J. Sinova, and T. Jungwirth, Phys. Rev. Lett. **109**, 076601 (2012).

[11] C. L. Degen, M. Poggio, H. J. Mamin, C. T. Rettner, and D. Rugar, Proc. Natl. Acad. Sci. U.S.A. **106**, 1313 (2009).

[12] I. Lee, Y. Obukhov, G. Xiang, A. Hauser, F. Yang, P. Banerjee, D. V. Pelekhov, and P. C. Hammel, Nature (London) **466**, 845 (2010).

[13] H. J. Mamin, M. Kim, M. H. Sherwood, C. T. Rettner, K. Ohno, D. D. Awschalom, and D. Rugar, Science **339**, 557 (2013).

[14] T. Staudacher, F. Shi, S. Pezzagna, J. Meijer, J. Du, C. A. Meriles, F. Reinhard, and J. Wrachtrup, Science **339**, 561 (2013).

[15] J. R. Maze, P. L. Stanwix, J. S. Hodges, S. Hong, J. M. Taylor, P. Cappellaro, L. Jiang, M. V. G. Dutt, E. Togan, A. S. Zibrov, A. Yacoby, R. L. Walsworth, and M. D. Lukin, Nature (London) **455**, 644 (2008).

[16] A. A. Khajetoorians, B. Baxevanis, C. Hbner, T. Schlenk, S. Krause, T. O. Wehling, S. Lounis, A. Lichtenstein, D. Pfannkuche, J. Wiebe, and R. Wiesendanger, Science **339**, 55 (2013).

[17] F. Meier and B. P. Zakharchenya, *Optical Orientation* (North-Holland, Amsterdam, 1984).

[18] M. A. Topinka, B. J. LeRoy, R. M. Westervelt, S. E. J. Shaw, R. Fleischmann, E. J. Heller, K. D. Maranowski, and A. C. Gossard, Nature (London) **410**, 183 (2001).

[19] J. Berezovsky, M. F. Borunda, E. J. Heller, and R. M. Westervelt, Nanotechnology **21**, 274013 (2010).

[20] Supplemental Material at http://link.aps.org/supplemental/ 10.1103/PhysRevLett.111.117201 for details of the sample, optical set-up for measuring spin PL, signal processing, and numerical techniques used for fitting and deconvolution.

[21] V. P. Bhallamudi, A. J. Berger, D. E. Labanowski, D. Stroud, and P. C. Hammel, J. Appl. Phys. **111**, 013902 (2012).

[22] R. Jansen, B. C. Min, S. P. Dash, S. Sharma, G. Kioseoglou, A. T. Hanbicki, O. M. J. van 't Erve, P. E. Thompson, and B. T. Jonker, Phys. Rev. B **82**, 241305(R) (2010).

[23] J. Russ, *The Image Processing Handbook* (CRC Press, Boca Rotan, FL, 2011).

[24] J.-D. Tournier, F. Calamante, D. G. Gadian, and A. Connelly, NeuroImage **23**, 1176 (2004).

[25] P. Basser, J. Mattiello, and D. LeBihan, Biophys. J. **66**, 259 (1994).

[26] K. M. Jansons and D. C. Alexander, Inverse Probl. **19**, 1031 (2003).

[27] I. Žutić, J. Fabian, and S. Das Sarma, Phys. Rev. B **64**, 121201 (2001).

[28] M. Holub, J. Shin, D. Saha, and P. Bhattacharya, Phys. Rev. Lett. **98**, 146603 (2007).